Multicomponent Transport in Nanoporous Networks: Theory and Simulation

Chunxia Hu[a,b], Suresh K. Bhatia[a]*

[a] School of Chemical Engineering, the University of Queensland, Brisbane, QLD 4072, Australia

[b] School of Materials Science and Engineering, Northwestern Polytechincal University, Xi'an, 710072, China

Abstract

We present a new theory to estimate fluxes and effective transport conductances of binary mixtures through a membrane comprising a nonuniform porous medium with both pore size and pore length distributions, using the Onsager formulation at the single pore level. The theory defines a conductance of each species that is dependent on the concentration gradients of the various species, and on using effective medium theory determines the fluxes and concentration profiles self-consistently in the porous medium. The transport of CH_4/H_2 mixtures in a silica membrane having a known pore size distribution is examined using this theory, and the results compared with those from rigorous simulations, showing good agreement. It is found that an optimal network coordination number exists at which species fluxes are a maximum, due to the opposing effects of increasing porosity and mean pore length with increase in coordination number. Further, network fluxes decrease with increase in pore dispersion, indicating that uniform pore size is optimal. A species and pressure-dependent optimal temperature is also predicted, due to the competing effects of increase in diffusivity and decrease in adsorption on increasing temperature. It is seen that the CH_4 selectivity is very sensitive to temperature, and undergoes a cross-over, with the membrane being more selective to CH_4 at low temperature and to H_2 at high temperature. In general, the selectivity is very sensitive to the distribution of pore volume, and for bimodal pore networks, undergoes a sharp transition at the percolation threshold, when the smaller pore size is impermeable to the larger species, CH_4. The approach offers a convenient adaption of effective medium theory to multicomponent systems with nonlinear isotherms, overcoming drawbacks of existing theory.

Keywords: porous network, binary mixture transport, effective medium theory, oscillator model, Maxwell-Stefan equation

* To whom correspondence may be addressed. Tel.: +61 7 3365 4263, Email: s.bhatia@uq.edu.au

1. Introduction

The understanding of multicomponent transport in porous media is of great interest due to its fundamental importance to a variety of applications in industry, for example, adsorptive separations, gas-solid reactions, and electrochemical processes. In recent years, interest has been significantly enhanced because of emerging novel technologies in industrial separation [1, 2], a wide variety of new applications in nanofluidics [3, 4], adsorptive energy storage [5, 6] and lab-on-a-chip technology [7], and the associated explosive growth of new nanoporous materials. Such materials include zeolites-based membranes [8, 9], carbon nanotubes [10, 11], metal organic frameworks [12], MCM-41 silica and their analogues [13], all of which are considered promising in the above applications. All the above applications involve the infiltration of fluids in highly confined spaces, which has stimulated efforts to understand the influence of structural characters and process conditions on the transport behaviour. An accurate fluid transport model is essential for the design of new porous materials and processes for specific applications, as well as for optimal operation.

The first step of the modelling processes is to describe the diffusion at the single pore level, for which the most common approach dates back to the works of Knudsen [14] and von Smoluchowski [15] almost a century ago. They treated the low-density transport of hard sphere molecules travelling in micron-sized channels, assuming diffuse wall reflection; nevertheless, this approach has been widely used even at the nanoscale without justification. The dusty gas model (DGM) [16-19], popular in modelling multicomponent transport in porous media, considers both diffusive and viscous resistances, with the former being a superposition of Knudsen and activated surface diffusion resistances, and molecular diffusion resistance, and the latter following the classical Poiseuille flow model. However, the Knudsen model inherits the weakness of the hard sphere representation, whereby the effects of dispersive interactions are overlooked. Moreover, DGM lacks a firm molecular foundation [19], and

semi-empirical fitting parameters are often introduced to obtain better agreement with experimental results [20, 21]. Recently, however, new theoretical models considering more accurate fluid-solid interactions have emerged, such as the oscillator model [22] and the distributed friction model [23, 24], as well as the Maxwell-Stefan (M-S) equation based approach [25-27]. Developed from statistical-mechanical principles, the oscillator model considers the trajectories of particles oscillating in the fluid-solid potential field at low density conditions, while undergoing diffuse wall collisions. Both the oscillator model and molecular dynamics simulations have shown the Knudsen model to significantly overpredict diffusion coefficients in nanoscale pores due to its neglect of the dispersive interactions [22, 25-28]. Simple correlations based on the oscillation model in idealised geometries have been derived for fast estimation and easy application [28]. The distributed friction model introduces the fluid-wall momentum exchange in the repulsive region of the fluid-solid potential through a pure component phenomenological friction coefficient, and considers the inhomogeneity of the adsorbate density profiles, providing novel insight into multicomponent transport analysis at the nanoscale. The M-S equation based approach is based on species concentrations within the accessible pore space, and indirectly considers the adsorption field through the pure component transport coefficients, which may be obtained by experiment or MD simulation.

With the diffusivity in each pore clearly expressed, a fluid transport model may be obtained by combining the information of pore network and connectivity. An established way to do this is effective medium theory (EMT) [29-31], by replacing a nonuniform network with distributed conductances by an effective network with a uniform transport conductance. However, EMT has the drawback of unknown tortuosity in a randomly oriented network, which is usually taken as an empirical fitting factor. An alternative method is the correlated random walk theory (CRWT) [32-34], which determines

the tortuosity of randomly oriented networks, by considering the correlation between successive pores traversed during the meandering of molecules in the pore network of uniform coordination number. A hybrid EMT-CWRT approach has subsequently been developed that overcomes the weakness of CRWT at the percolation threshold, and provides better agreement with simulation [35]. The hybrid approach has been used to explain the experimental variation of apparent tortuosity with temperature in mesoporous membranes for single species [36], as well as the influence of the network morphology on the diffusion of fluid mixtures in porous media [37]. A simulation-based alternative to describe the transport in the porous media involves solving the mass conservation balances in a network with a given pore size distribution and coordination number, and has been applied by several researchers [37-42]. Nevertheless, the computational demand of the simulations is large, and an appropriate numerical method is required to ensure global convergence for multicomponent transport.

In this work, a new approach to analyse binary transport of mixtures in porous material or membrane is developed, which combines the oscillator model for pure components and the M-S equation based approach for the single pore transport with a hybrid EMT-CWRT method for the pore network transport, to determine mixture species fluxes in a non-uniform pore network. In this theory, for computational advantage we use the correlation based on the oscillator model to account for soft-sphere transport in the pores [28], while the M-S equation provides an efficient way to determine pore level individual species fluxes in multicomponent transport based only on the information of pure component diffusivities. To validate this theory, simulations are conducted in which the mass conservation equations at each node, based on application of the generalized M-S model [25, 43, 44] in the connecting pores in a nonuniform pore network, are numerically solved to provide as the solution of the problem of transport in the porous medium. The theoretical and simulation results are shown to

be in good agreement. Further, the variation of the structural parameters and operating conditions is shown to lead to a rich variety of behaviour of the fluxes, discussed in detail in this article. Although the approach is presented in the context of binary mixture transport, it is quite general in concept and can be readily extended to mixtures with more than two components.

2. Modelling Binary Mixture Transport in a Porous Network

2.1 Transport in a single pore

At the single pore level, we use the M-S equation for binary diffusion in a single pore, following [25]

$$-\frac{c_i}{R_g T}\frac{d\mu_i}{dx} = \sum_{\substack{j=1 \\ j\neq i}}^{n} \frac{c_j j_i - c_i j_j}{c_t Đ_{ij}} + \frac{j_i}{Đ_i}; \quad i = 1,2 \tag{1}$$

where, T is temperature, R_g is the ideal gas constant, x is flow direction of species in the pore, μ_i, c_i and j_i are chemical potential, adsorbed concentration and flux of species i, respectively, and c_t is the total adsorbed molar concentration of the two species. $Đ_{ij}$ is the M-S exchange coefficient for binary diffusion, and $Đ_i$ is the M-S diffusivity for molecule-wall interactions. We define a matrix of Onsager coefficients, $\boldsymbol{\Omega}$, which satisfies

$$j_i = -\sum_{j=1}^{2} \Omega_{ij} \frac{d\mu_j}{dx}; \qquad i = 1,2 \tag{2}$$

Combining Eq. (1) and (2), after some manipulation, leads to

$$\begin{aligned} \Omega_{ii} &= \frac{c_i c_t R_j Đ_i Đ_{ij}}{R_g T\left(R_i R_j - c_i c_j Đ_i Đ_j\right)} \quad , \quad i, j = 1,2. \;\; j \neq i \\ \Omega_{ij} &= \frac{c_i c_j c_t Đ_i Đ_j Đ_{ij}}{R_g T\left(R_i R_j - c_i c_j Đ_i Đ_j\right)} \quad , \quad i, j = 1,2. \;\; j \neq i \end{aligned} \tag{3}$$

where, $R_i = c_t Đ_{ij} + c_j Đ_i$. Assuming ideal gas, Eq. (2) can be rearranged to the Fickian form [26]:

$$\begin{aligned} j_i &= -D_i \frac{dc_{bi}}{dx} \\ D_i &= R_g T\left(\frac{\Omega_{ii}}{c_{bi}} + \frac{\Omega_{ij}}{c_{bj}}\frac{dc_{bj}/dx}{dc_{bi}/dx}\right) \end{aligned} \tag{4}$$

where c_{bi} is a pseudo-bulk concentration representing the bulk concentration of species i that would be in equilibrium with the local adsorbed mixture having local concentrations c_1, c_2. We now define the species-specific transport conductance, λ, for a cylindrical pore with radius r and length l:

$$\lambda = \frac{\pi r^2 D}{l} \tag{5}$$

such that the flow rate of species i through the pore, F_i, is given by

$$F_i = \lambda_i(-\Delta C_{bi}) \tag{6}$$

This leads to the transport conductance for species i, in the presence of the other species in the mixture, in a single pore:

$$\lambda_i = \pi R_g T \frac{r^2}{l}\left(\frac{\Omega_{ii}}{c_{bi}} + \frac{\Omega_{ij}}{c_{bj}}\frac{dc_{bj}/dx}{dc_{bi}/dx}\right) \tag{7}$$

The advantage of the above formulation in Eqs. (6) and (7) is that by imbedding the gradient of the other species within the conductance, λ_i, for any species i, it provides a system of coupled transport equations in single component format, that can be conveniently averaged over a pore network.

2.2 Transport in pore networks

The above single pore conductance must be suitably averaged over the pore size and length distribution to obtain the local transport parameters of a pore network that may exist in a porous material or membrane. To this end, we use EMT, which replaces the network by an equivalent network having pores of uniform conductance. Thus, at the network level, the local pore size-dependent conductance λ_i of species i in Eq. (7) is replaced by a uniform transport conductance λ_{ie}, i.e.

$$\lambda_{ie} = \pi R_g T \left\langle \frac{r^2}{l}\left(\frac{\Omega_{ii}}{c_{bi}} + \frac{\Omega_{ij}}{c_{bj}}\frac{dc_{bj}/dx}{dc_{bi}/dx}\right)\right\rangle_{eff} \tag{8}$$

where $\langle \bullet \rangle_{eff}$ represents an effective value, considering the distribution of pore radii and lengths. In a porous medium or membrane the concentrations c_1, c_2 are position-dependent, as a result of which the

conductances are also position-dependent. We consider a network of randomly oriented pores having a uniform coordination number, N, which represents the number of pore segments meeting at an intersection. Following EMT, the flux of species i in the effective medium having pores of uniform conductance λ_{ie} is given by [31, 35]

$$J_i = -\frac{\varepsilon \left\langle l^2 \right\rangle \lambda_{ie}}{\pi \gamma \left\langle r^2 l \right\rangle} \frac{dc_{bi}}{dz} \tag{9}$$

where z represents the coordinate along the macroscopic diffusion direction, ε is the porosity of the network, and γ is a tortuosity given by [34]

$$\gamma = \frac{3(N+1)}{(N-1)} \tag{10}$$

Equations (8) and (9) lead to the local effective medium transport conductance for species i in a porous network as

$$\lambda_{ie}(z) = \pi R_g T \left\langle \frac{r^2}{l} \left(\frac{\Omega_{ii}}{c_{bi}} + \frac{\Omega_{ij}}{c_{bj}} \frac{J_j \lambda_{ie}}{J_i \lambda_{je}} \right) \right\rangle_{eff} \tag{11}$$

where we have assumed

$$\frac{dc_{bi}/dx}{dc_{bj}/dx} = \frac{dc_{bi}/dz}{dc_{bj}/dz} \tag{12}$$

Equation (12) may be expected to hold provided the pore lengths are much smaller than the macroscopic dimensions of the porous medium or membrane. The local effective transport conductance of species i, $\lambda_{ie}(z)$, follows from EMT as the solution to the nonlinear equation [31, 35]

$$\int_0^\infty \int_0^\infty \frac{\lambda_{ie}(z) - \lambda_i(z,r,l)}{\left[\lambda_i(z,r,l) + (N/2-1)\lambda_{ie}(z)\right]} f(r,l)\,dr\,dl = 0 \tag{13}$$

where $f(r,l)$ is a joint pore radius and length number probability distribution, and

$$\lambda_i(z,r,l) = \pi R_g T \frac{r^2}{l} \left(\frac{\Omega_{ii}}{c_{bi}} + \frac{\Omega_{ij}}{c_{bj}} \frac{J_j \lambda_{ie}}{J_i \lambda_{je}} \right) \tag{14}$$

Here we note that at the level of the porous medium the pseudo-bulk concentrations c_{b1}, c_{b2} are position-dependent, as a result of which the conductances are also position-dependent. In principle, the EMT result in Eq. (13) is strictly valid only for an infinitely large system. Nevertheless, this condition is practically met if the pore lengths are sufficiently small compared to the macroscopic system size, so that the species concentrations can be approximated as linearly varying over the pore length. The solution to Eq. (13) then provides a position dependent effective medium conductance $\lambda_{ie}(z)$. We note that the local individual pore scale conductances in Eq. (14) depend on the macroscopic fluxes, J_i, in the medium, and therefore on the local macroscopic concentration gradients, dc_{bi}/dz, following Eq. (9). Thus, the local effective medium conductance is correlated with the macroscopic transport in the porous material, and both sets of equations must be solved simultaneously as a coupled system. In the subsequent section we address the macroscopic transport, to complete the model description.

As an alternative to the above approach, henceforth termed T1, we also consider a recent EMT-based theory of transport in pore networks [37], in which effective mixture Onsager coefficients are locally obtained in place of the effective conductance for each species in T1. In this theory, termed T2, the exchange part of the two species is treated separately, leading to a transport conductance matrix $\boldsymbol{\lambda}$, which satisfies

$$\lambda_{ij} = \pi R_g T \frac{r^2}{l} \frac{\Omega_{ij}}{c_{bj}} \quad , \quad i, j = 1, 2 \tag{15}$$

for a pore with pore radius r and pore length l. This can be derived from the flux, expressed in Fickian form as

$$\mathbf{j} = -\mathbf{D} \frac{d\mathbf{c_b}}{dx} \tag{16}$$

For binary mixture transport, $\mathbf{j} = \begin{bmatrix} j_1 & j_2 \end{bmatrix}^T$, $\mathbf{c_b} = \begin{bmatrix} c_{b1} & c_{b2} \end{bmatrix}^T$, and $\mathbf{D}$ is the diffusivity matrix $\left\{D_{ij}\right\}_{i,j=1,2}$

$$D_{ij} = R_g T \frac{\Omega_{ij}}{c_{bj}}, i, j = 1,2 \tag{17}$$

In the multicomponent EMT [37] an effective conductance matrix, $\boldsymbol{\lambda}_\mathbf{e}$, is defined such that

$$J_i = -\frac{\varepsilon \left\langle l^2 \right\rangle}{\pi\gamma \left\langle r^2 l \right\rangle} \sum_j \lambda_{e,ij} \frac{dc_{bj}}{dz} \tag{18}$$

The local effective transport conductance matrix, $\boldsymbol{\lambda}_\mathbf{e}$, is the solution to the coupled nonlinear system of equations [37]

$$\int_0^\infty \int_0^\infty \left(\left(\frac{N}{2} - 1 \right) \boldsymbol{\lambda}_\mathbf{e} + \boldsymbol{\lambda} \right)^{-1} \left(\boldsymbol{\lambda}_\mathbf{e} - \boldsymbol{\lambda} \right) f(r,l) dr dl = \mathbf{0} \tag{19}$$

This provides a system of four coupled nonlinear equations for the different components of the 2x2 matrix $\boldsymbol{\lambda}_\mathbf{e}$. Based on the solution for $\boldsymbol{\lambda}_\mathbf{e}$ the species fluxes can now be determined for the porous medium, as elaborated in the next section.

2.3 Transport at the membrane scale

As an application of the present approach (T1), and the earlier method (T2), we consider a flat membrane exposed to a mixture having concentrations $c_{bi,in}$ and $c_{bi,out}$ at the retentate and permeate ends respectively. To obtain the fluxes J_i and the concentration profiles of the species in the membrane, in the case of T1 we integrate Eq. (9) to formally write

$$c_{bi}(z) = c_{bi,in} - \frac{\pi\gamma \left\langle r^2 l \right\rangle J_i}{\varepsilon \left\langle l^2 \right\rangle} \int_0^z \frac{1}{\lambda_{ie}(z')} dz' \quad , \quad i = 1,2 \tag{20}$$

$$J_i = \frac{c_{bi,in} - c_{bi,out}}{\frac{\pi\gamma \left\langle r^2 l \right\rangle}{\varepsilon \left\langle l^2 \right\rangle} \int_0^L \frac{dz'}{\lambda_{ie}(z')}} \quad , \quad i = 1,2 \tag{21}$$

where L is the thickness of the porous network or membrane. Given any pore size and length distribution, $f(r,l)$, and expressions for the pore scale Onsager coefficients in terms of local pseudo-

bulk mixture compositions, Eqs. (9), (10) and (13), (14), (20), (21) may be readily solved to obtain the profiles of concentration and effective conductance as well as membrane flux of each species. Equation (3) relates the pore scale Onsager coefficients to the mixture composition and the M-S diffusivities, models for which are discussed in the next section.

In applying the earlier approach, T2, described in Eqs. (15)-(17) and (19), the fluxes J_i and the concentration profiles of species in the network are obtained upon integration of Eq. (18) as

$$c_{bi}(z) = c_{bi,in} + \frac{\pi\gamma\left\langle r^2 l\right\rangle}{\varepsilon\left\langle l^2\right\rangle}\int_0^z \frac{J_j\lambda_{ij,e}(z') - J_i\lambda_{jj,e}(z')}{Q(z')}dz' \quad , \quad i,j = 1,2 \tag{22}$$

$$J_i = -\frac{\varepsilon\left\langle l^2\right\rangle}{\pi\gamma\left\langle r^2 l\right\rangle}\frac{\left(c_{bi,in}-c_{bi,out}\right)\int_0^L \frac{\lambda_{ii,e}(z')}{Q(z')}dz' + \left(c_{bj,in}-c_{bj,out}\right)\int_0^L \frac{\lambda_{ij,e}(z')}{Q(z')}dz'}{\int_0^L \frac{\lambda_{ji,e}(z')}{Q(z')}dz'\int_0^L \frac{\lambda_{ij,e}(z')}{Q(z')}dz' - \int_0^L \frac{\lambda_{jj,e}(z')}{Q(z')}dz'\int_0^L \frac{\lambda_{ii,e}(z')}{Q(z')}dz'} \quad , \quad i,j = 1,2 \tag{23}$$

where, $Q(z) = \lambda_{ii,e}(z)\lambda_{jj,e}(z) - \lambda_{ij,e}(z)\lambda_{ji,e}(z)$. As shown by Bonilla and Bhatia [37] the matrix, $\boldsymbol{\lambda}_{\mathbf{e}}$, is symmetric, so that $\lambda_{ij} = \lambda_{ji}$.

2.4 Single pore isotherms and diffusion coefficients

Solution of the above model requires specifications of the mixture isotherms relating the adsorbed concentrations c_i to the pseudo-bulk concentrations, and suitable models for the diffusion coefficients. While our approach is more generally applicable, for convenience we assume a Langmuir isotherm for each species, following

$$c_i = \frac{b_i c_{i,sat} p_i}{(1+\sum_{j=1}^{n} b_j p_j)} \tag{24}$$

with $c_{i,sat} = c_{j,sat} = \varepsilon\rho(8.5988 - 0.0156T)$, corresponding to the value for several gases on H-Mordenite [45]. Here T is in K and $c_{i,sat}$ in mol/m^3, ε is the porosity, and ρ is the porous medium density in g/cm^3. The Langmuir equilibrium constant b_i varies with pore size, and is assumed to follow the Van't Hoff form

$$b_i = b_{0i} \exp\left(-\phi_i(r)/RT\right) \tag{25}$$

where b_{0i} is the affinity constant of species i at zero energy level, and $\phi_i(r)$ is the adsorption energy, defined as the minimum interaction potential between species i and the wall of a cylindrical pore radius r [37]. Following Tjatjopoulos et al. [46] the interaction potential is expressed as

$$U(x^*, R^*) = \varepsilon_{fs} n^* \pi^2 \left[\frac{63}{32} \frac{1}{x^{*10}\left[2 - \frac{x^*}{R^*}\right]^{10}} F\left[-\frac{9}{2}, -\frac{9}{2}; 1; \left(1 - \frac{x^*}{R^*}\right)^2\right] - 3 \frac{1}{x^{*4}\left[2 - \frac{x^*}{R^*}\right]^{4}} F\left[-\frac{3}{2}, -\frac{3}{2}; 1; \left(1 - \frac{x^*}{R^*}\right)^2\right] \right] \tag{26}$$

where, x^* is the dimensionless distance of closest approach between the fluid molecule and the cylindrical surface, R^* is the radius of the cylinder scaled with σ_{fs}, and $F[\alpha, \beta; \gamma; z]$ denotes the hypergeometric series with parameters α, β, γ. $n^* = n\sigma_{fs}^2$ and n is the density of the pore wall (atoms per unit volume). σ_{fs} and ε_{fs} are the solid-fluid collision diameter and the solid-fluid Lennard-Jones potential well depth respectively, evaluated using the Lorentz-Berthelot mixing rules.

The M-S diffusivity $Đ_i$ is expressed by a simple correlations based on the oscillator model for diffusion in nanopores developed in this laboratory [22, 28]

$$Đ_i = r_p \sqrt{\frac{k_B T}{m_i}} D_{0i}^* \tag{27}$$

where, m_i is the mass of species i, k_B is the Boltzmann constant, r_p is half of the center-to-center pore diameter and D_{0i}^* is the dimensionless diffusivity of species i. The M-S diffusivity $Đ_i$ is taken as the diffusivity in a pore of radius r_p, following the Oscillator model [22], whose solution is available in the form of correlations for D_{0i}^* [28]. For the binary exchange coefficient, $Đ_{ij}$, we assume that fluid-solid interactions dominate, as occurs in nanoscale pores and, following Krishna and van Baten [25], we use the correlation

$$c_t Đ_{ij} = c_{i,sat} Đ_i^{c_i/(c_i+c_j)} Đ_j^{c_j/(c_i+c_j)} \quad (28)$$

3. Simulation

For validation of the above theoretical approach, simulations were done on synthetically generated random pore networks having an arbitrary pore size distribution and uniform coordination number, spanning the space between the two sides of a membrane. The Maxwell-Stefan model was applied at the pore level, and conservation equations at each node were then used to solve for the pore fluxes, and ultimately determine the overall flux of each species in the membrane. In the simulation, a pore network was generated within a medium formed by $n_c \times n_c \times n_c$ cubic cells with $l_c=L/n_c$ as the cube length. The surface nodes were located on the surface of the surface cells at the retentate side and the permeate side and directly connected to the next inner nodes by pores of random size, to provide the pathways from the interior pore network to the surface. An inner node was randomly located inside each cell and joined to N neighbours by pores of random size, establishing the interior pathways for gas transport. More information of how this network is realized is available elsewhere [37]. Thus, with membrane thickness L and cube length l_c, the number of nodes is the summation of inner nodes ($n_c \times n_c \times n_c$) and surface nodes ($2 \times n_c \times n_c$). The number of pores is the summation of inner pores ($[n_c \times n_c \times n_c \times N / 2]$) and surface pores ($n_c \times n_c$).

Figure 1(a) depicts a schematic diagram of one-dimensional transport through a porous membrane, illustrating the transport at macroscale with total pressures P_{in} at the retentate side and P_{out} at the permeate side, while Figure 1(b) shows an example of the pore network in the membrane with $5 \times 5 \times 5$ inner nodes and coordination number 6.

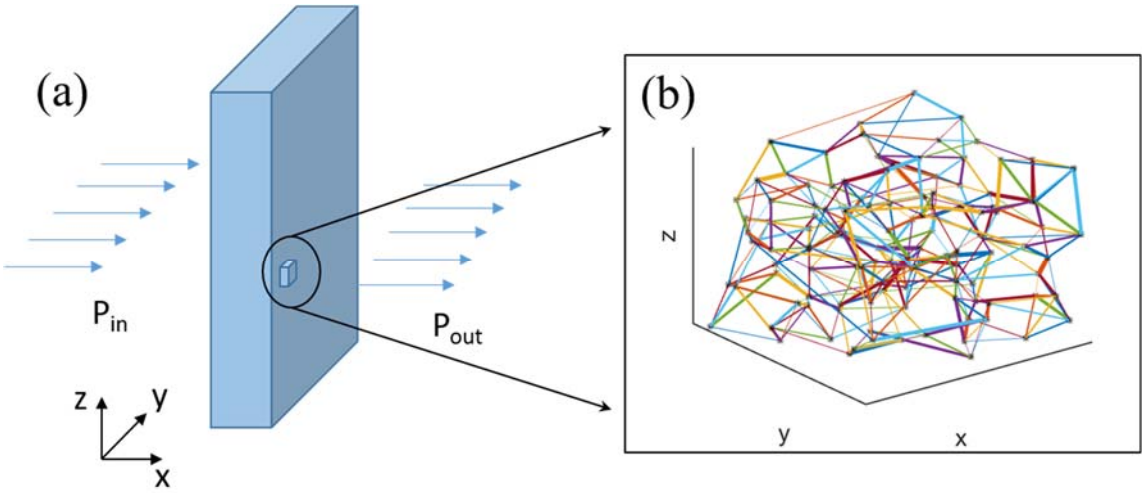

Figure 1. (a) Schematic of one-dimensional transport through a porous membrane, with total pressure P_{in} at the retentate side and P_{out} at the permeate side, and (b) an example of random network in the membrane with $5\times5\times5$ cubic cells and coordination number 6. The stars represent the location of nodes, while colored lines denote the pores and line thickness is proportional to pore radius.

To obtain the fluxes in the network, it is necessary to simultaneously solve the single pore transport equations in all pores of the network, with the condition of mass conservation at each node [37]. To this end we recast Eq. (1) in Fickian form, leading to

$$\mathbf{j} = -\mathbf{B}^{-1}\boldsymbol{\Gamma}\frac{d\mathbf{p}}{dz} \tag{29}$$

where,

$$\mathbf{p} = \left[p_1, p_2\right]^T, \quad \boldsymbol{\Gamma} = \mathbf{diag}\left(c_i / p_i\right) \tag{29a}$$

$$B_{ij} = \begin{cases} \displaystyle\sum_{\substack{j=1 \\ j\neq i}}^{n} \frac{c_j}{Đ_{ij}} + \frac{1}{Đ_i}, & i = j \\ \displaystyle -\frac{c_i}{c_t Đ_{ij}}, & i \neq j \end{cases} \tag{29b}$$

It is assumed that the fraction coverage and transport properties are evaluated at an average partial pressure p_i (pseudo-bulk partial pressure) in a single pore and thus they are constant at the single pore level. The transport conductance matrix for pore i is written as

$$\boldsymbol{\lambda}_i = \frac{\pi r_i^2}{l_i}\mathbf{B}^{-1}\boldsymbol{\Gamma} \tag{30}$$

Following the mass conservation law, at inner node *j* where *N* pores meet, the flow rates satisfy

$$\sum_{k=1}^{N} \boldsymbol{\lambda}_{jk} \left(\mathbf{p}_k - \mathbf{p}_j \right) = \mathbf{0} \tag{31}$$

where, $\mathbf{p}_k$ is the partial pressure vector at node *k*. Repeating Eq. (31) for every inner node in the network leads to a set of equations of the form

$$\mathbf{G}\mathbf{x} = \mathbf{b} \tag{32}$$

Here, for a network of *M* inner nodes

$$\mathbf{G} = \begin{bmatrix} \sum_{\mathbf{k=2}}^{M} \boldsymbol{\lambda}_{\mathbf{1k}} + \boldsymbol{\lambda}_{\mathbf{10}} + \boldsymbol{\lambda}_{\mathbf{1L}} & -\boldsymbol{\lambda}_{\mathbf{12}} & \cdots & -\boldsymbol{\lambda}_{\mathbf{1M}} \\ -\boldsymbol{\lambda}_{\mathbf{21}} & \sum_{\substack{\mathbf{k=1} \\ \mathbf{k\neq 2}}}^{\mathbf{M}} \boldsymbol{\lambda}_{\mathbf{2k}} + \boldsymbol{\lambda}_{\mathbf{20}} + \boldsymbol{\lambda}_{\mathbf{2L}} & & \vdots \\ \vdots & & \ddots & \\ -\boldsymbol{\lambda}_{\mathbf{M1}} & \cdots & & \sum_{\mathbf{k=1}}^{\mathbf{M-1}} \boldsymbol{\lambda}_{\mathbf{Mk}} + \boldsymbol{\lambda}_{\mathbf{M0}} + \boldsymbol{\lambda}_{\mathbf{ML}} \end{bmatrix} \tag{33}$$

$$\mathbf{b} = \begin{bmatrix} \boldsymbol{\lambda}_{\mathbf{10}} \mathbf{p}_{in} + \boldsymbol{\lambda}_{\mathbf{1L}} \mathbf{p}_{out} \\ \vdots \\ \boldsymbol{\lambda}_{\mathbf{M0}} \mathbf{p}_{in} + \boldsymbol{\lambda}_{\mathbf{ML}} \mathbf{p}_{out} \end{bmatrix} \quad \text{and} \quad \mathbf{x} = \begin{bmatrix} \mathbf{p}_1 \\ \vdots \\ \mathbf{p}_M \end{bmatrix} \tag{34}$$

Upon solution of Eq. (32) to obtain the partial pressure matrix in the network, the flow rates at the retentate side and permeate side of the membrane are obtained as:

$$\begin{aligned} \mathbf{F}_{\mathbf{in}} &= \sum_{\mathbf{k=1}}^{\mathbf{M^{2/3}}} \boldsymbol{\lambda}_{\mathbf{k0}} \left(\mathbf{p}_{in} - \mathbf{p}_k \right) \\ \mathbf{F}_{\mathbf{out}} &= \sum_{\mathbf{k=M-M^{2/3}}}^{\mathbf{M}} \boldsymbol{\lambda}_{\mathbf{kL}} \left(\mathbf{p}_k - \mathbf{p}_{out} \right) \end{aligned} \tag{35}$$

This leads to the flux matrix for the membrane

$$\mathbf{J} = \frac{\mathbf{F}_{\mathbf{in}} + \mathbf{F}_{\mathbf{out}}}{2 s_{surface}} \tag{36}$$

where, $s_{surface}$ is the surface area of the membrane normal to the flow direction.

4. Results and Discussions

In order to validate the theoretical approach presented in Section 2 against simulations as described above, and to investigate the sensitivity to process parameters, we consider the transport of a CH_4/H_2 mixture in a silica porous network having an arbitrary pore size distribution. The parameters used in the theory and simulation are listed in Table 1.

Table 1: Parameters used in the calculations

	silica	CH_4	H_2
σ_{ss} or σ_{ff} (nm)	0.28	0.381	0.2915
ε_{ss}/k_B or ε_{ff}/k_B (K)	492.7	148.2	38.0
b_{0i} (kPa^{-1})	--	7.485e-5	3.355e-4
solid density (kg/m^3)	2320	--	--

For the joint number probability density of pore radius and length, we assume that the radius and length are uncorrelated and independently distributed. Both continuous and discrete pore sizes distribution are considered in this study. For the continuous case, we use the Rayleigh distribution

$$p_c(r) = \frac{r/r_a - s}{r_a(1-s)^2} \exp\left[-\frac{1}{2}\left(\frac{r/r_a - s}{1-s}\right)^2\right] \tag{37}$$

for the open pore radius (i.e. accessible pore radius), r, where $s = r_0/r_a$ is the size dispersion parameter, and r_a and r_0 are the modal and minimum pore radius, respectively. Unless otherwise indicated, in all calculations to be discussed for a continuous pore size distribution we used the base case membrane structural parameter values $N = 6$, $s = 0.16$, $r_0 = 0.4$ nm, and membrane thickness $L = 500$ nm. Further, the network was generated using a cube length value $l_c = 20$ nm.

For the discrete case, a bimodal distribution with porosity ratio $e = \varepsilon_1/\varepsilon_2$ and pore size ratio $u = r_1/r_2$ is considered, leading to the pore size distribution

$$p_b(r) = m\delta(r - r_1) + (1-m)\delta(r - r_2) \tag{38}$$

where m is the normalized frequency of pore size r_1, given by $m = e/(e+u^2)$, and δ is the Dirac delta function. These distributions were also used in constructing the network in the simulations, with random pore sizes based on these distributions. During the construction, the porosity of the network is obtained based on the actual pore network by

$$\varepsilon = \frac{\sum_n \pi r_i^2 l_i}{L^3} \tag{39}$$

where n is the total number of the pores in the network. In the theory, the pore length distribution, $p(l)$, is taken as the average of the conditional length probabilities of the N neighbours to a reference point in a uniform distribution of random points [40]. The pore length is related to the coordination number N and the length, l_c, of the cube in which a node is randomly located, and $< l >= \int_0^\infty lp(l)dl$ is the mean pore length. Unless otherwise discussed, for discrete pore size distributions we used the parameter values $N = 6$, $u = 10$ and $r_1 = 4.0$ nm, $l_c = 20$ nm, and membrane thickness $L = 500$ nm. In both the continuous and discrete pore size distributions all pores were part of the same network, and there were no independent micropore or macropore networks.

Figure 2 depicts the variations of the porosity with membrane thickness, average pore length, coordination number and size dispersion parameter and the relationship between l_c, $<l>$ and N, which are useful for the discussion below. From Figures 2(a) and 2(b) it is evident that the porosity is only weakly sensitive to membrane thickness, while it is more strongly dependent on cube length, l_c, coordination number, N, and dispersion in pore size distribution, s. This sensitivity of porosity to membrane thickness is largely due to end effects, since the pores connecting surface nodes to the interior nodes break the symmetry of the interior structure and can have a slightly different length distribution. These end effects disappear with increase in membrane thickness, and are largest at small

cube length l_c (Figure 2(a)). The average pore length is smaller than the cube length when the coordination number is less than 9, as shown in Figure 2(c).

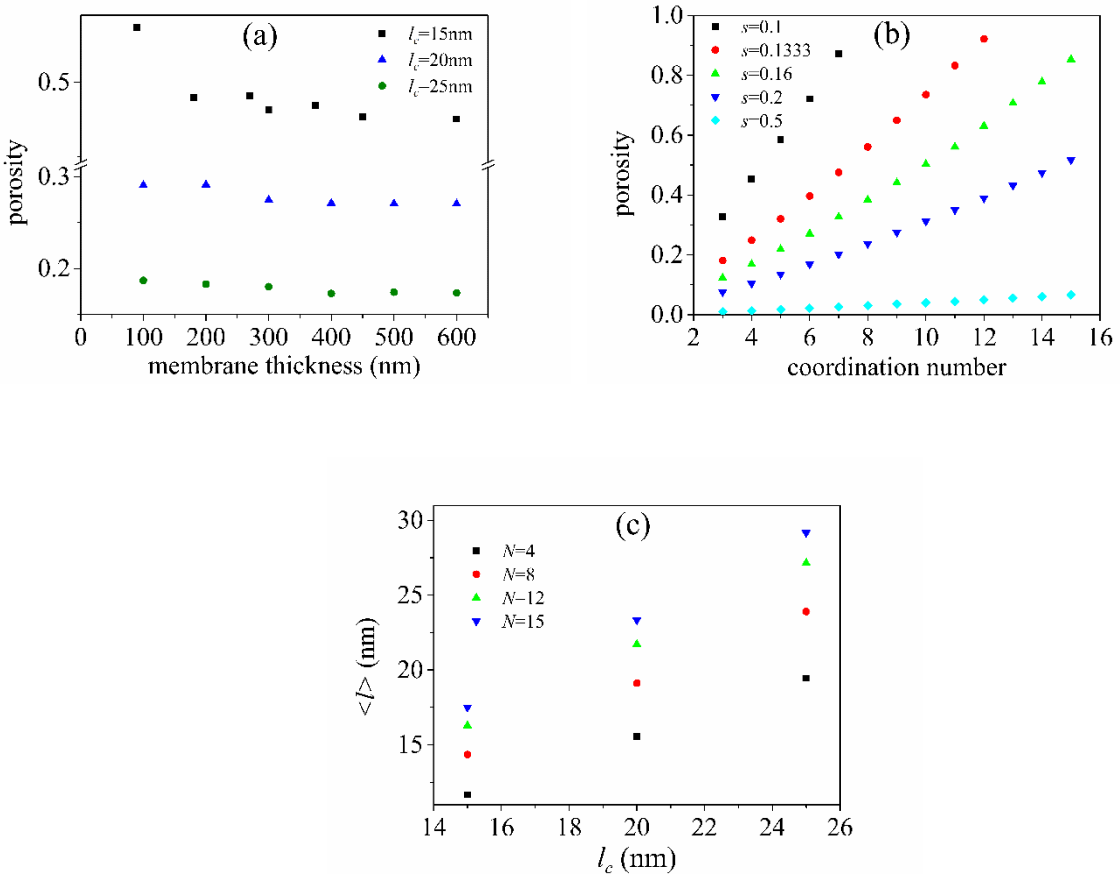

Figure 2. (a) Variation of porosity with membrane thickness and cube length, (b) variation of the porosity with coordination number and size dispersion parameter, and (c) variation of the average pore length <*l*> with cube length l_c, for a network with continuous pore size distribution.

4.1 Continuous pore size distribution

4.1.1 Comparison between theory and simulation

We first report our comparisons between theory and simulations, demonstrating the validity of the approach developed here. To solve the coupled membrane model equations for a binary mixture it is required to specify both inlet and outlet partial pressures of each species. For the inlet we specify the inlet total pressure, P_{in}, and mole fraction of CH_4, x_{in}, while the outlet conditions are determined by specifying the total pressure drop, ΔP, and defining a variable x_Δ such that the outlet partial pressure

of CH_4 is given by $\left(x_{in}P_{in} - x_{\Delta}\Delta P\right)$, and that of H_2 by $\left[(1-x_{in})P_{in} - (1-x_{\Delta})\Delta P\right]$. For all calculations reported here, unless otherwise specified we use the base case operating parameter values T = 300 K, P_{in} = 200 kPa, x_{in} = 0.5 and x_{Δ} = 0.5, with ΔP taking on various values, as specified in each figure. Figure 3(a) depicts the variation of H_2, CH_4 membrane fluxes with Rayleigh distribution parameter $s=r_0/r_a$ in a network with coordination number N=6, r_0=0.4 nm, cube length l_c=20.0 nm and thickness L=500 nm. The operating conditions of the membrane are: T = 300 K, P_{in} = 200 kPa with mole fraction of CH_4 x_{in}= 0.5, total pressure drop ΔP =100 kPa, and x_{Δ}=0.5. The solid lines in the figure represent the results from the present theory T1, and the dash lines those from the earlier theory T2. It is clear that while both the theories do reasonably well in comparison with the simulation, T1 performs better at smaller s, that is, for wider pore size distributions. Figure 3(b) shows the variation of the fluxes with coordination number in a network with Rayleigh distribution parameters of s=0.16, r_0=0.4 nm, l_c=20.0 nm and L=500 nm at the same operating conditions, showing good agreement among both theories and simulation. The theories predict correct trends with the simulation with increase of the coordination number. A slight overestimation of the fluxes by the theories occurs when the coordination number is larger than 11, due to the fact that, in the simulation, a connection to its ith neighbour will force a more distant node to be connected for large coordination numbers. The mathematic form of pore length distribution used in the theory is not catching all the behaviours in the simulation. Figure 3(c) shows the variation of the fluxes with membrane thickness in a network with Rayleigh distribution of s=0.16, r_0=0.4 nm, l_c=20.0 nm and N=6. The theories display good agreement with the simulation, except when the membrane thickness is small, at 50 nm. In that case, EMT is inaccurate because the pore length is not negligible in comparison to the membrane thickness, and the assumption of an infinitely large network that underlies the EMT is violated. While we have shown here the results for a large pressure drop of 100 kPa our calculations for a small pressure drop of 0.02 Pa gave similar quality of agreement

between theory and simulation as Figure 3. It should be mentioned that although the two theories gave the same results at most conditions, T1 is computationally more expedient, involving only nonlinear equations instead of matrixes and their inverses, and is somewhat faster in execution. For T1, usually about 15 iterations are needed to get a result, while for T2, about 35 are needed. The calculation time (with i7-2600 CPU @ 3.40GHz) of either theory for a single point is less than five minutes, while that for the simulation is several hours depending on the pore number of the network. This clearly demonstrates the computational advantage, by more than an order of magnitude, of the present theory over simulation, which is attractive given that it is also accurate and matches simulation.

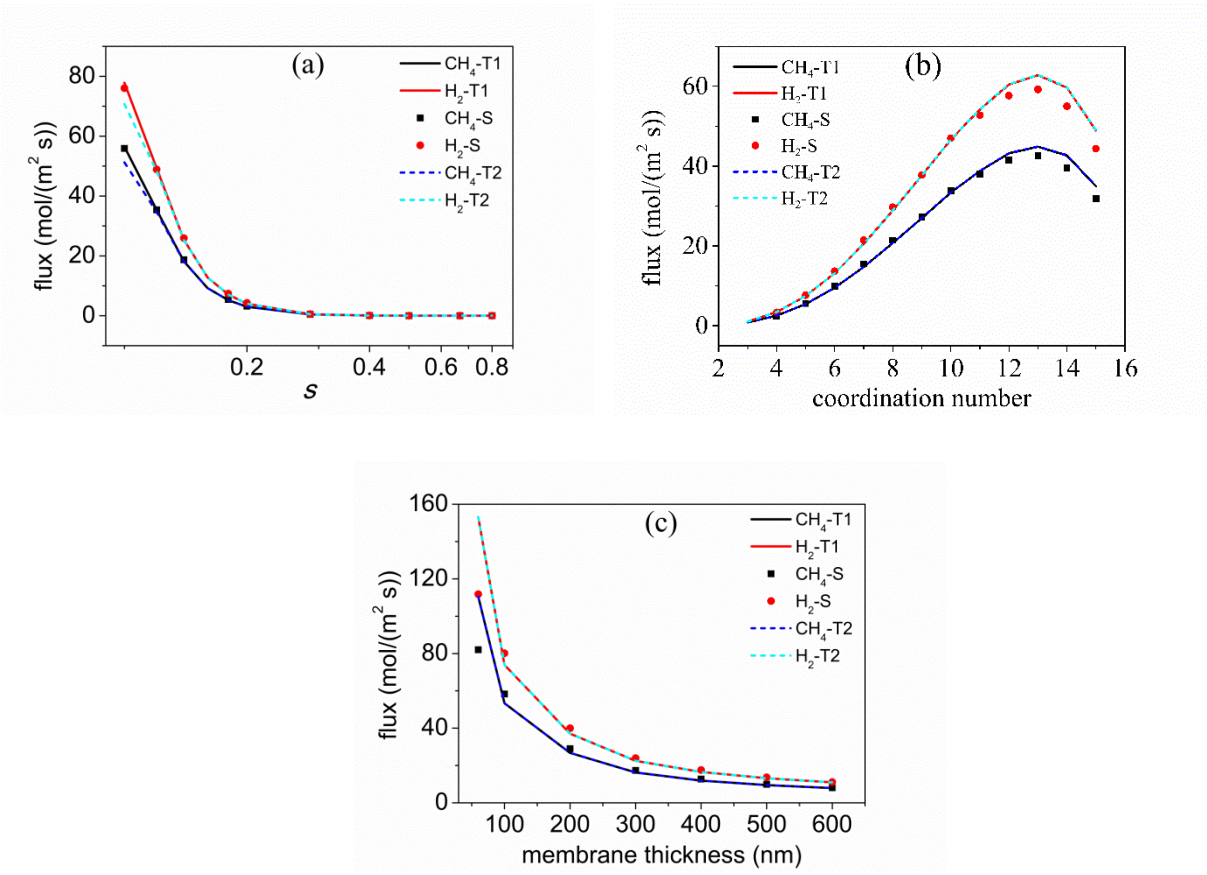

Figure 3. Comparison of the variation of theoretical and simulation-based fluxes with (a) Rayleigh distribution parameter $s=r_0/r_a$, (b) coordination number, and (c) membrane thickness. S stands for simulation, while T1 is the present theory and T2 is the earlier theory [37].

4.1.2 Effect of the membrane parameters

In this part, the membrane parameters, such as the size dispersion parameter of Rayleigh distribution s, the coordination number N, the membrane thickness L and the cube length l_c, were studied to investigate their influences on the binary mixture transport. As the fluxes at both small and large pressure drop show similar information for different membrane parameters, only the results for small pressure drop are listed and discussed. Figure 4 depicts the variation of the fluxes with membrane thickness and cubic length at T=300 K, P_{in}=200 kPa with mol fraction of CH_4 x_{in}=0.5, ΔP =0.02 Pa and x_Δ=0.5 in a network with Rayleigh distribution of s=0.16 and r_0=0.4 nm. When the cube length increases, the average pore length increases as shown in Figure 2(c). However, the fluxes increase with the decrease of the cube length. This is due to the increasing number of pores included in a membrane, leading to increase of the porosity, as shown in Figure 2(a). When the porosity increases, the saturation concentration in mol per volume of the membrane increases, leading to a higher flux. The decrease of the membrane flux is expected when the membrane thickness increases at a total constant pressure drop, as the pressure drop per unit length decreases. The slower decrease at large membrane thicknesses is due to the effect of the porosity. According to Eq. (21), the flux is proportional to the porosity, which decreases slowly at large membrane thicknesses as shown in Figure 2(a). The porosity shows a more apparent effect on the membrane flux than the cube length, leading to a higher flux at a smaller cube length. Specifically, the fluxes at porosity 0.475 with l_c=15 nm and porosity 0.187 with l_c=25 nm are similar, illustrating the increasing influence of the porosity, as well as the decreasing effect of the average pore length, on the membrane fluxes.

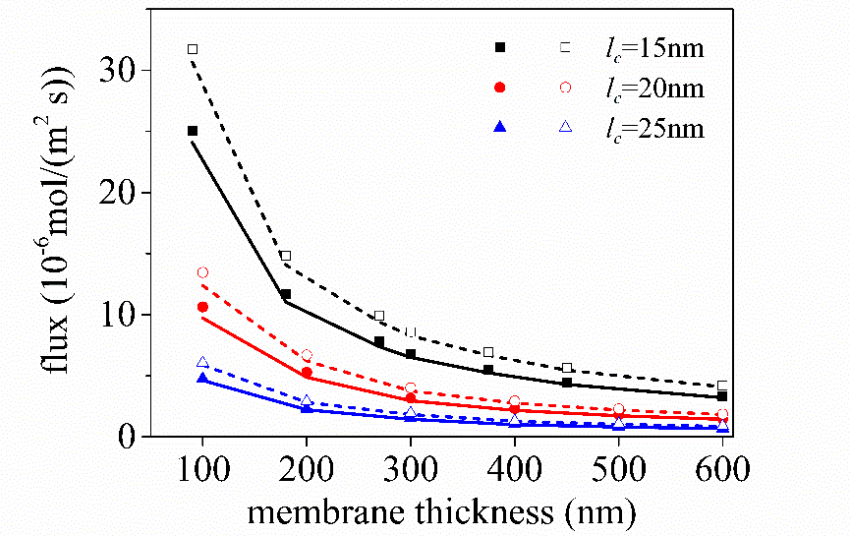

Figure 4. Variation of the fluxes with membrane thickness and cube length. Solid and dashed lines represent CH_4 and H_2 fluxes from the present theory, while solid and hollow symbols are CH_4 and H_2 fluxes from simulation.

Figure 5 depicts the variation of the fluxes with coordination number at 300 K, P_{in}=200 kPa with mol fraction of CH_4 x_{in}=0.5, ΔP =0.02 Pa and x_Δ=0.5 in a network with l_c=20 nm and various Rayleigh distributions. An optimal coordination number is shown for every pore size distribution, where the membrane fluxes attains a maximum value. From the porosity-coordination number relation in Figure 2(b) it is estimated that the maxima of the fluxes are located at a porosity $\varepsilon \approx 0.72$, which can be considered the optimal porosity. When the coordination number increases, the porosity increases, as can be seen in Figure 2(b), which leads to increase in flux. However, the average pore length also increases with coordination number, as more nodes are linked together at a constant cell length, following Figure 4, which has an opposite effect on the flux. A maximum in flux therefore occurs, as consequence of these opposing effects, as the coordination number increases. Figure 6 depicts the variation of the effective conductance at the retentate side of the membrane at the same parameters in Figure 5. As the pressure drop considered here is very small, the effective conductances at different positions vary only slightly, and can be represented by the values at the retentate side. The effective conductance also has a maximum value with the variation of the coordination number, consistent with

a maximum in flux, following Eq. (21). However, the values of the coordination number at which the flux and the effective conductance reach the maximum are slightly different. This is due to the decrease of the factor $\langle r^2 l \rangle / \varepsilon l^2$ with increase in coordination number, leading to a maximum in flux at a coordination number larger than that for the maximum in conductance. As seen in Figures 5 and 6 the optimum coordination number is rather large for *s* larger than 0.1, and exceeds the range of 3-6 commonly observed for porous materials [47]. From a practical viewpoint therefore a coordination number of 6 may be a realistic target for pore size distributions corresponding to s > 0.1.

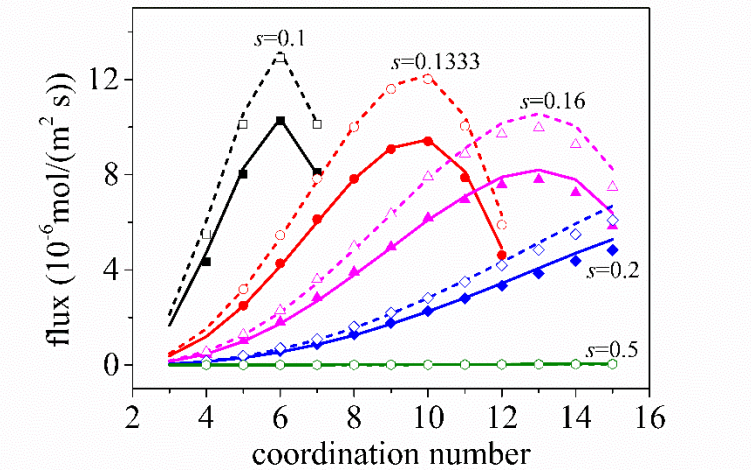

Figure 5. Variation of the fluxes with coordination number for various values of s. Solid and dashed lines represent CH_4 and H_2 fluxes from the present theory, while solid and hollow symbols are CH_4 and H_2 fluxes from simulation.

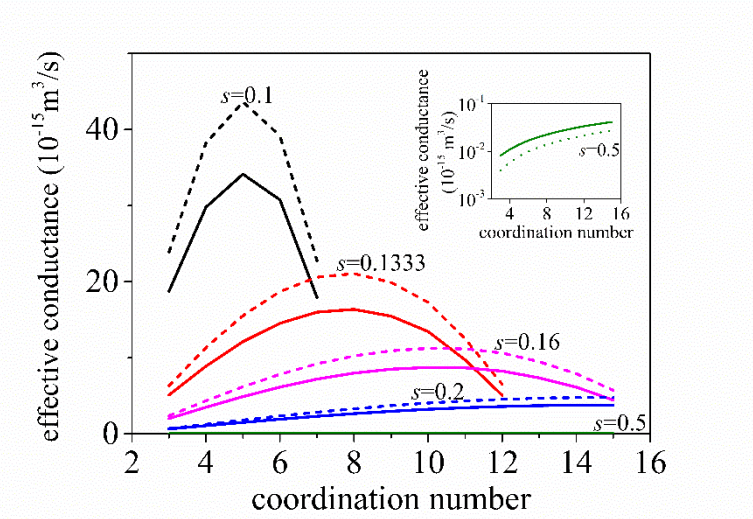

Figure 6. Variation of the effective conductance on the retentate side with coordination number. The parameters are the same as for Fig. 5. Solid and dashed lines represent CH_4 and H_2 effective conductances from the present theory.

We note here that for the pore size distributions considered, with r_0 = 0.4 nm all of the pores are accessible to even the larger molecule (CH_4). In this case, our advancement of EMT to extend it to multicomponent systems is very successful, and shows good agreement with exact simulations. From earlier studies with pure component systems [35], for which the EMT is originally developed, it is known that EMT is inaccurate when the fraction of accessible pores is close to the threshold, and significant deviation between theory and simulation may be therefore expected for sufficiently small r_0 and large s for which the percolation threshold is approached. However, since the aim of the present work is to extend the EMT to multicomponent systems in the region where it is accurate, and not to overcome this weakness of EMT, the latter was not investigated here. Clearly, the shortcoming of EMT in the neighbourhood of the percolation threshold will also apply to the present approach for multicomponent transport, as it does for the pure component case.

4.1.3 Effect of operating conditions

In this part, the effects of operation conditions, pressure and temperature, were studied. Figure 7 depicts the variation of the fluxes and selectivity (flux of CH_4/flux of H_2) with temperature, at different inlet total pressures with mol fraction of CH_4 x_{in}=0.5, constant total pressure drop ΔP =100 kPa and x_Δ=0.5. The membrane is 500 nm thick with Rayleigh distribution parameters of s=0.16, r_0=0.4 nm, l_c=20 nm and N=6. The total pressure drop is kept very small, so that the pseudo-bulk pressure may be considered constant. It should be mentioned that at large total pressure drop, as long as the pressure drop in a single pore is small enough to be viewed as a constant, the present theory and simulation work properly. It is seen in Figure 7(a) that the theoretical results are in very good agreement with simulation. The fluxes decrease with the increase of the total pressure at all temperatures, which is the result of the increase of the pseudo-bulk concentration. When the pseudo-bulk concentration increases, the adsorbed concentration increases, leading to a slower decrease at higher total pressures. Temperature

change shows more complex effects, with a maximum flux at different temperatures for each of the two species. An increase of temperature enhances the pure component diffusion coefficient for any species, inducing higher flux in the membrane. On the other hand, the equilibrium constant b_i for each species decreases with increase in temperature, following Eq. (25), leading to reduced concentration of the species in the pores, and therefore to lower values of the diagonal terms of the thermodynamic factor matrix $\boldsymbol{\Gamma}$ based on Eqs. (24) and (29a). This tends to reduce the flux, following Eq. (29), and the opposing effects of diffusivity increase and decrease in adsorbed concentration with increase in temperature leads to the maximum in flux. However, as shown in Figure 7(b), the CH_4/H_2 flux selectivity shows a continuous decrease with increase in temperature, which is due to the higher temperature of the maximum for H_2, and stronger increase in its flux compared to CH_4 below this temperature maximum. It is seen in Figure 7(b) that increase of the total pressure leads to a very slight increase of the selectivity, indicating that the temperature has a more noteworthy effect. From Figure 7(b) it is evident that the membrane is more selective to CH_4 at low temperature, and to H_2 at high temperature, with the selectivity cross-over dependent on the operating pressure.

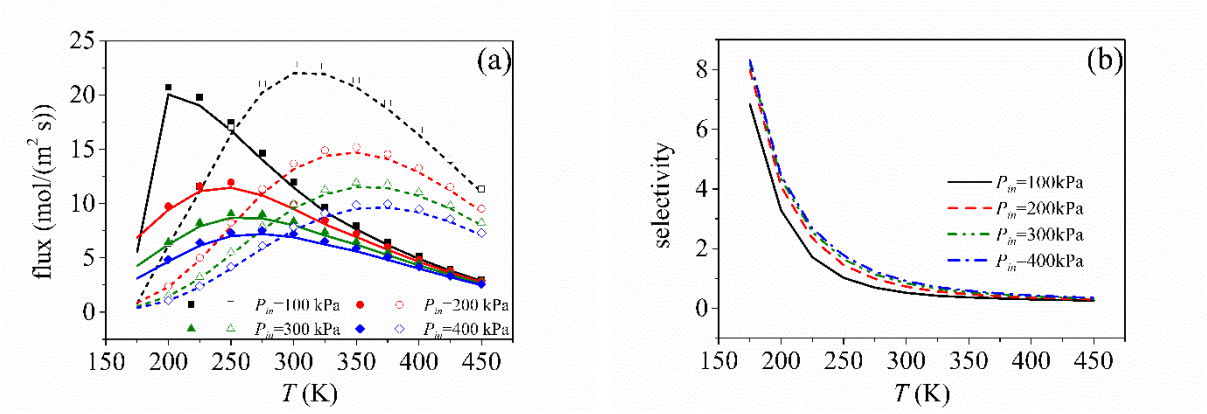

Figure 7. Variation of the (a) fluxes, and (b) selectivity (flux of CH_4/flux of H_2) with temperature, for ΔP =100 kPa. In (a), solid and dashed lines represent CH_4 and H_2 fluxes from present theory, solid and hollow symbols are CH_4 and H_2 fluxes from simulation.

Figure 8 depicts the variation of the flux and CH_4/H_2 selectivity with mole fraction of CH_4 at the retentate side at 300 K, P_{in}=100, 200, 300 and 400 kPa, constant total pressure drop ΔP =20 kPa and

x_Δ=0.5. The membrane parameters are the same as those in Figure 7. As seen in Figure 8(a) the flux of hydrogen decreases dramatically with increase of the bulk mole fraction of methane. As the methane molecules are larger and heavier than hydrogen molecules, the pure component methane diffusivity is smaller than that of hydrogen, leading to reduction in the MS binary diffusion coefficient on increasing methane mole fraction, following Eq. (28). This leads to increased drag on H_2 and reduction in H_2 flux with increase in mole fraction of methane. On the other hand the drag effect of the faster diffusing but much lighter H_2 is very small on CH_4, and only a weak effect on CH_4 flux is seen on increasing CH_4 mole fraction. As seen in Figure 8(b) the CH_4/H_2 therefore selectivity correspondingly increases with increase in mole fraction methane. An interesting related feature is the existence of a weak maximum in the flux of CH_4 with increase in its mole fraction at low total pressure, as seen in Figure 9, which again arises from the competitive effects of the binary MS diffusivity and the thermodynamic factor Γ. Actually, the increasing of the methane diffusion can also be viewed in the methane flux, when the methane pressure is not so large, which is clearly shown in Figure 9.

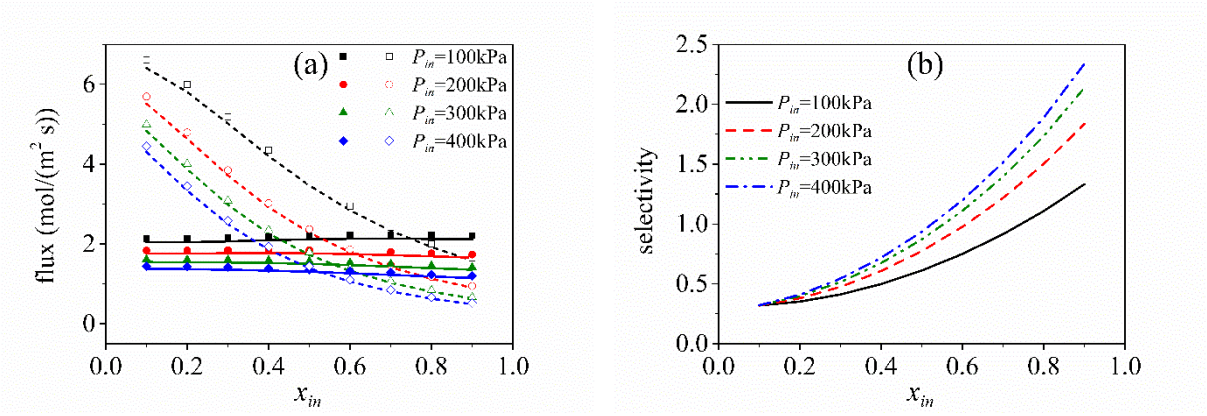

Figure 8. Variation of (a) fluxes, and (b) CH_4/H_2 selectivity with mole fraction of CH_4 at the retentate side x_{in}, at constant total pressure drop ΔP =20 kPa. In (a), solid and dashed lines represent CH_4 and H_2 fluxes from present theory, while solid and hollow symbols are CH_4 and H_2 fluxes from simulation.

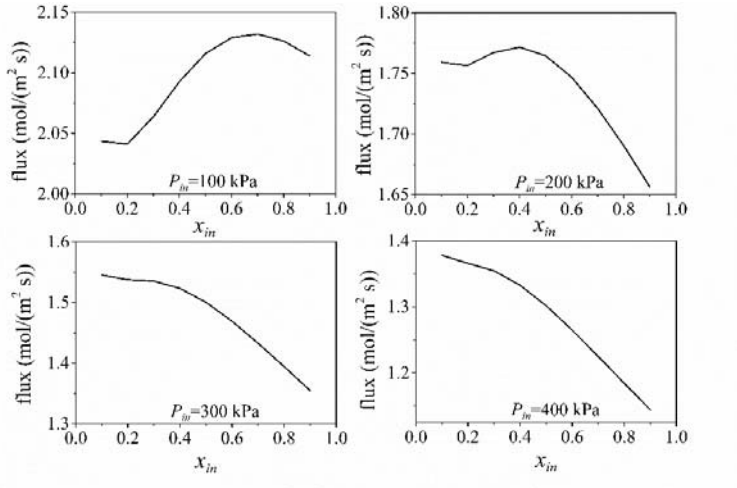

Figure 9. Variation of methane flux with mole fraction of CH_4, x_{in}. The parameters are the same as in Figure 8.

Figure 10 depicts the variation of fluxes and effective conductance at the retentate side with x_Δ, for various values of x_{in}, , at 300 K, P_{in}=200 kPa and constant total pressure drop ΔP =0.02 Pa. The membrane is 500 nm thick with pore network a Rayleigh distribution parameters of s=0.16, r_0=0.4nm, l_c=20.0nm and N=6. Very good agreement with simulation is seen at all values of x_Δ. Here small pressure drop is taken to permit a complete variation of x_Δ, and to show the effect of interaction between the gases more directly. As seen in Figure 10(a), there is a cross-over of the curves for CH_4, indicative of the drag effect of H_2. At low values of x_Δ the partial pressure drop of CH_4 is low, and therefore the flux of CH_4 is also low, while that of H_2 is high. On increasing x_Δ the flux of CH_4 increases, however this increase is steeper at low values of x_{in} for which the mole fraction and flux of H_2 is high, and this leads to a cross-over of the curves of methane flux for different values of x_{in} at a value of x_Δ of about 0.4. Thus, as is to be expected higher mole fractions of H_2 leads to increase of its drag on CH_4. As is evident in Figure 10(b) this drag of H_2 also leads to cross-over in the effective conductance curves of CH_4 with variation in x_Δ. Further, there is a large decrease in effective conductance of CH_4 at small x_Δ and large increase in effective conductance of H_2 at large x_Δ, as shown in Figure 10(b). The changes imply increase in effective conductance of each component with increase in its mole fraction.

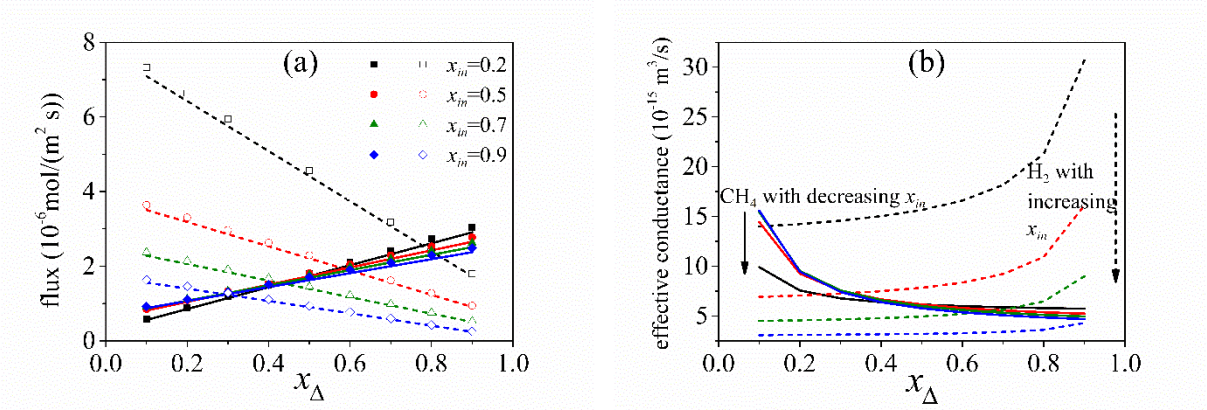

Figure 10. Variation of (a) fluxes, and (b) effective conductance at the retentate side, with x_Δ for various values of x_{in}, and constant total pressure drop ΔP =0.02 Pa. In (a), solid and dashed lines represent CH_4 and H_2 fluxes from present theory, while solid and hollow symbols are CH_4 and H_2 fluxes from simulation. In (b), solid and dashed lines represent effective conductance of CH_4 and H_2 at the retentate side from present theory.

4.2 Discrete pore size distribution

To highlight percolation effects and accuracy of the approach when they are important, we next investigated a discrete pore size distribution, assuming the pore size distribution to comprise two distinct sizes, r_1 and r_2. If pores with radius r_2 are inaccessible to species i, that is $\lambda_i(r_2)=0$, following Eqs. (13) and (38) EMT yields

$$\lambda_{ie}=\left(\frac{\frac{N}{2}m-1}{\frac{N}{2}-1}\right)\lambda_i(r_1) \tag{40}$$

leading to a percolation threshold $m=2/N$ i.e., $e=2u^2/(N-2)$.

Figure 11 depicts the variation of the fluxes with porosity ratio e at 300 K, P_{in}=200 kPa with x_{in}=0.5 and ΔP =100 kPa with x_Δ=0.5 in a network N=6 and with a bimodal distribution of u=10 and r_1=4.0 nm. The solid and dashed lines in the figure represent the present theory and the earlier theory [37], while the symbols represent the simulation results, showing good match between the theories and simulation. Since the smallest center-to-center pore diameter is larger than the solid-fluid collision diameters, all the pores are accessible to the two species. A steep flux drop occurs near the percolation

threshold $e_p = 50$, especially for methane, as sufficient small pores are present for $e_p < 50$ that there can be no pathway in the network that avoids the 0.4 nm radius smaller pore that has the much lower diffusion coefficient compared to the larger pore of size r_1=4.0 nm. With decrease in e below 50 there is a much more gradual drop in the flux of each component, evident from both theory and simulation. For $e > e_p$, there are paths in the network that contain no small pore and the number of such paths gradually increases as e increases, leading to an increase in flux of each species.

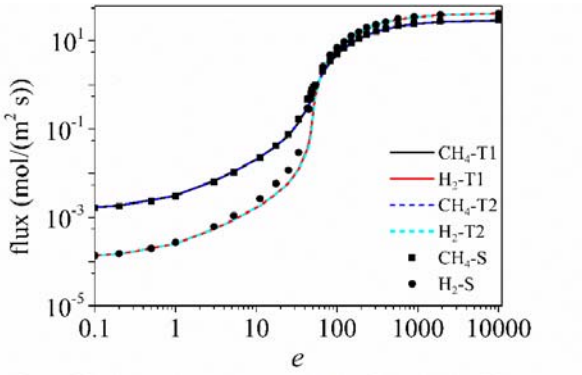

Figure 11. Variation of fluxes with porosity ratio e at 300 K and ΔP =100 kPa, for a network with a bimodal pore size distribution. S stands for simulation, while T1 is the present theory and T2 is the earlier theory [37].

Figure 12 depicts the variation of the fluxes and selectivity with porosity ratio e for r_1=1.8 nm, r_2=0.18 nm, and N=4, 6, 9. The other parameters are the same as in Figure 11. In this case pores with radius r_2 are inaccessible to methane. The flux of methane drops dramatically down to zero at the percolation threshold, because there is no path through the network that avoids the smaller pore. The selectivity is zero for $e < e_p$ and constant for $e > e_p$ in Figure 12(b), which is the result of zero flux of methane for $e < e_p$ and comparable flux of CH_4 and H_2 for $e > e_p$. Simulations were also conducted for the parameters used in Figure 12, however convergence was very slow and difficult to achieve when the porosity is small and the percolation threshold is approached; nevertheless, the theory shows good agreement with the available simulation results away from the threshold, as seen in Figure 12(a).

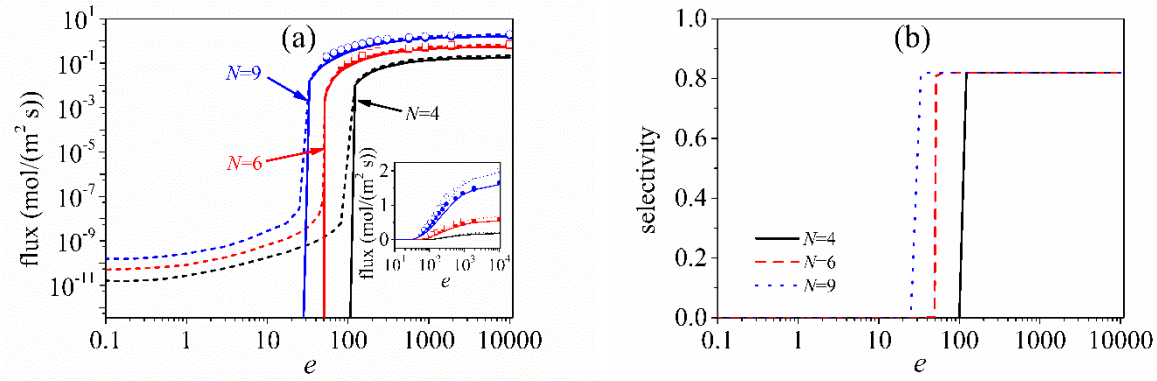

Figure 12. Variation of the fluxes (a) and selectivity (flux of CH_4/ flux of H_2) (b) with porosity ratio e at 300 K and ΔP =100 kPa in a network with a bimodal pore size distribution. In (a), solid lines and solid symbols are CH_4 fluxes from theory and simulation, while dashed lines and hollow symbols are those of H_2. The small difference between the gas fluxes on the upper branch is shown more clearly in the inset.

Figure 13 depicts the variation of the fluxes and selectivity with porosity ratio e for P_{in}=200 kPa with x_{in}=0.5 and ΔP =100 kPa with x_{Δ}=0.5 in a network with N=6, and a bimodal distribution with u=10 and r_1=1.8 nm (Figures 13(a) and 13(c)) and 4.0 nm (Figures 13(b) and 13(d)). Various temperatures have been tested in the theory, showing only a small influence on the fluxes with change in temperature when $e > e_p$ for the bimodal pore size distributions considered, as shown in Figure 13(a) and (b). The limited amount of the small pores is the main reason restricting the increase of the flux as the temperature increases. In the case of r_1=1.8 nm and r_2 = 0.18 nm, the selectivity increases dramatically at the percolation threshold as e increases due to the incorporation of paths avoiding the smaller pore that is inaccessible to CH_4, as seen in Figure 13(c). The larger pore is non-selective, as is evident from its selectivity of close to 1, and this reduces weakly with increase in temperature. In Figure 13(d) both pore sizes are permeable to CH_4, but every permeable path contains only the non-selective pore size of 4.0 nm for $e > e_p$, and so the selectivity suffers a sharp drop at the percolation threshold of e=50.

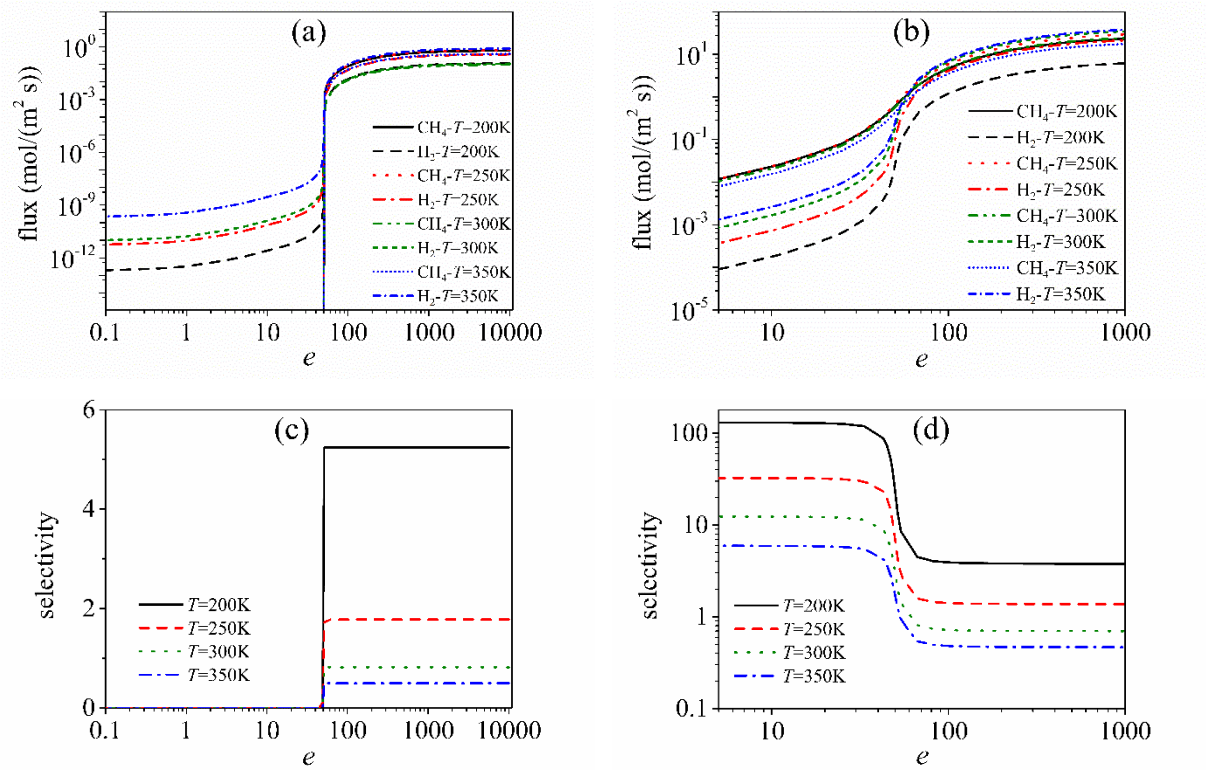

Figure 13. Variation of (a), (b) fluxes and (c), (d) selectivity (flux of CH_4/flux of H_2) with porosity ratio e at T=200 K, 250 K, 300 K, and 350 K and and ΔP =100 kPa with x_Δ=0.5 in a network with a bimodal pore size distribution.

Figure 14 depicts the variation of the fluxes and selectivity with porosity ratio at 300 K and different mole factions of CH_4. The other parameters are the same as those in Figure 13. It is seen in Figure 14(a) that when the smallest pores are inaccessible to methane, the flux of hydrogen remains nearly constant in the region of $e < e_p$, indicating that only single gas transport occurs in the pore network. The fluxes vary over a wider range in the region of $e < e_p$ when all pores are accessible to both species, as seen in Figure 14(b), due to the larger size of the smaller pore compared to that in 14(a). In the region of $e > e_p$, the flux of methane increases only weakly under both situations, as the gas molecules tend to follow the path of least resistance, i.e. paths avoiding the smaller pore in both cases. It is seen that the selectivity decreases with increase of the methane mole fraction. It is seen that the selectivity is constant with the variation of e in the region of $e < e_p$ or $e > e_p$, which is because the pathways

followed by gas molecules in the network from the inlet to the outlet are dominated by one of the two pore sizes, so that the porosity ratio has no effect on the selectivity of the membrane.

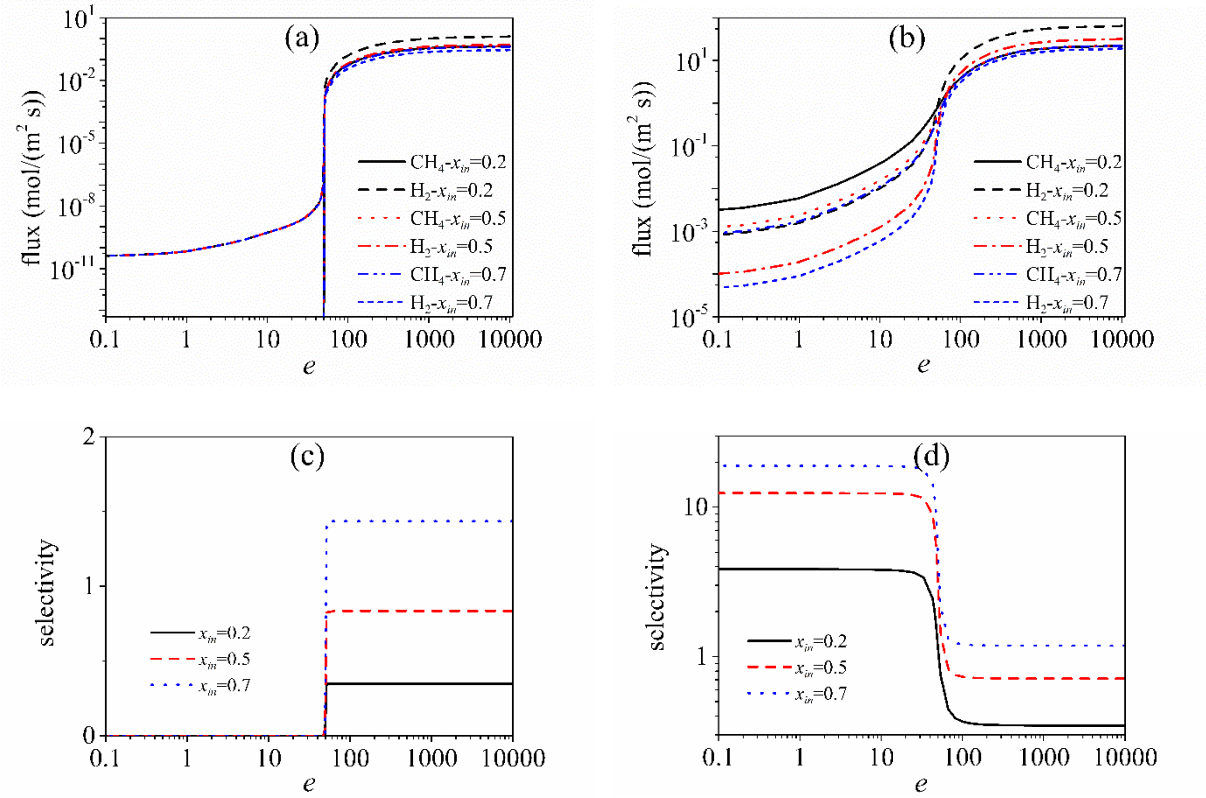

Figure 14. Variation of (a), (b) fluxes, and (c), (d) selectivity (flux of CH_4/ flux of H_2) with porosity ratio e at 300K, with x_{in}=0.2, 0.5 and 0.7, and ΔP =80 kPa, in a network with a bimodal pore size distribution for (a), (c) r_1=1.8nm, and (b) (d) r_1=4.0 nm.

When small pores are accessible to methane, i.e. r_2=0.4 nm, a strong nonlinear concentration profile for H_2 occurs at high H_2 partial pressure compared to CH_4, as seen in Figure 15, which depicts the variation of effective conductance, and of concentration, with the position in the pore network for ratio e=1 and 900.9, T=300K, P_{in}=200 kPa with x_{in}=0.2, 0.3, 0.5 and 0.7, and ΔP =80 kPa with x_Δ=0.5, in a network of coordination number N=6 and a bimodal distribution of u=10 and r_1=4.0 nm. Nonlinear conductance and concentration profiles for H_2 are seen for x_{in}=0.2 and 0.3, when e=1, while those for CH_4 show much weaker nonlinearity under all conditions. This effect clearly arises from the small pores of radius 0.4 nm, which predominate for e=1, while for the value of e=900.9 it is the large pores of radius 4 nm that predominate. This nonlinearity for e=1 is readily seen to be due to the drag of the

slower component CH_4 on the much more weakly adsorbing H_2 in the small pores. To verify this, we consider the ratio

$$\frac{c_{bi}\Omega_{ij}}{c_{bj}\Omega_{ii}} = \frac{c_{bi}C_j Đ_j}{c_{bj}R_j} = \frac{c_{bi}c_j Đ_j}{c_{bj}(c_t Đ_{ij} + c_i Đ_j)} \tag{41}$$

For the case when i corresponds to H_2, $c_j >> c_i$ since CH_4 is much more strongly adsorbed in the narrow pore of radius 0.4 nm, and $c_t Đ_{ij} \simeq c_{i,sat} Đ_j$ following Eq. (28). Further, since $c_i << c_{i,sat}$ due to the weak adsorption of H_2, Eq. (41) yields

$$\frac{c_{bi}\Omega_{ij}}{c_{bj}\Omega_{ii}} \simeq \frac{c_{bi}c_j}{c_{bj}c_{i,sat}} \tag{42}$$

which leads to the nonlinearity in the H_2 conductance and concentration profile when the pseudo-bulk concentration of H_2 is sufficiently large, as in the case of $x_{in} = 0.2$, due to the nonlinearity of the CH_4 isotherm. In this case the drag of CH_4 becomes dominant and reduces the conductance of H_2 at the retentate side, but this effect disappears at the permeate side where the mole fraction of CH_4 approaches zero for the value of $x_\Delta = 0.5$ used in Figure 15. As a result the conductance of H_2 increases towards the permeate side, leading to the nonlinearity in the concentration profile for H_2. By the same arguments, it is easily seen that the drag of H_2 on CH_4 is small, leading to relatively uniform conductance and nearly linear concentration profile for CH_4 in Figure 15(c). For larger values of x_{in} the effect of drag of CH_4 on H_2 becomes weaker, as the pseudo-bulk concentration of H_2, c_{bi}, reduces while the adsorbed concentration of CH_4 increases only slightly due to the small pores being nearly saturated. Consequently the nonlinearity of the hydrogen concentration profile reduced with increase in x_{in}. For the case of e=900.9 the large pores of radius 4.0 nm predominate, and both H_2 and CH_4 are now much more weakly adsorbed in comparison to that in 0.4 nm pores, with small Langmuir equilibrium constants, at the bulk pressures considered here. Under this condition the ratio in Eq. (42)

is significantly smaller than unity and drag of CH_4 on H_2 is negligible, and vice versa, leading to much smaller change in conductances and nearly linear concentration profiles in Figure 15(d).

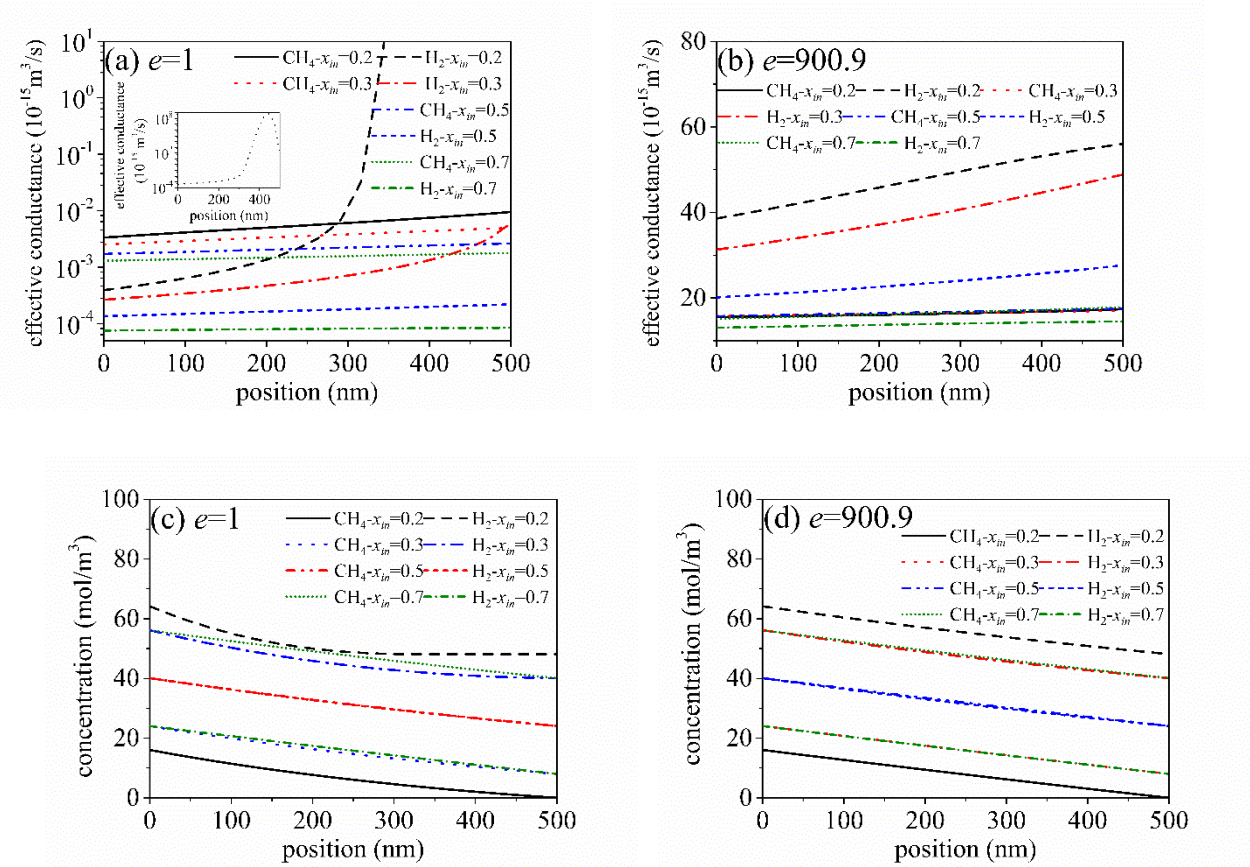

Figure 15. Variation of (a), (b) effective conductance, and (c), (d) concentration with the position in the pore network at ratio e=1, 900.9, T=300K, with x_{in}=0.2, 0.5 and 0.7, and ΔP =80 kPa, in a network with a bimodal pore size distribution.

Conclusion

A new theory to investigate the binary mixture diffusion in a membrane comprising a porous network with nonuniform pore sizes and pore lengths is presented, in which the local effective conductance is correlated with the macroscopic transport in the porous medium. The total flux in the network, the species effective conductance and concentration profiles along the network constitute a system of nonlinear equations that are solved self-consistently, and the results are compared against rigorous simulations of the network transport for a CH_4/H_2 mixture. The comparisons show very good agreement between theory and simulations for membranes having both continuous and discrete pore

size distributions. It is found that in finite membranes end effects lead to porosity loss with increase in membrane thickness, and this reduction is steeper at small membrane thickness. As a result, the flux decrease nonlinearly with increase in membrane thickness, with the effect being stronger at low membrane thickness. It is also seen that there is an optimal network coordination number for maximum flux or effective conductance of each species, due to the competing effect of increase in porosity and increase in mean pore length on increasing coordination number. Further, the flux of each species reduces on increasing the dispersion in the pore size distribution, suggesting that narrow pore size distributions are advantageous for enhancing permeability.

Investigation of the effect of operating conditions on the fluxes and selectivities of the H_2/CH_4 mixture reveals that the fluxes are a maximum at an optimal temperature that depends on the species, due to the competing influences of increase in diffusivities and decrease in amounts adsorbed on increase in temperature; however, the CH_4/H_2 selectivity reduces on increase in temperature, with the membrane being more selective for H_2 at high temperature while being selective to CH_4 at low temperature. The temperature at which the cross-over in selectivity from CH_4 to H_2 occurs depends on the operating pressure. Further, for bimodal pore size distributions, the transport is well-predicted when compared to simulation, even in the vicinity of the percolation threshold, attesting to the power of the approach. When the porosity ratio of the two pore sizes is varied, the selectivity experiences a sharp change when one of the two pore sizes crosses its percolation threshold, consistent with expectation. When the pores are accessible to both species, concentration and effective conductance profiles along the network shows clear evidence of nonlinearity, arising from the differential mobility of the two species, with the slower moving CH_4 exerting a drag effect on the hydrogen that depends on the operating pressure and the gas composition. The method developed offers a convenient formulation to adapt effective medium theory to multicomponent transport in systems having nonlinear isotherms.

Acknowledgements

This research has been supported by a grant (No. DP150101996) from the Australian Research Council, through the Discovery scheme. Chunxia Hu gratefully acknowledges the financial support of CSC (China Scholarship Council) scholarship.

References

[1] S. Krause, V. Bon, I. Senkovska, U. Stoeck, D. Wallacher, D.M. Többens, S. Zander, R.S. Pillai, G. Maurin, F.o.-X. Coudert, S. Kaskel, A pressure-amplifying framework material with negative gas adsorption transitions, Nature 532 (2016) 348-352.

[2] F. Soyekwo, Q. Zhang, R. Gao, Y. Qu, C. Lin, X. Huang, A. Zhu, Q. Liu, Cellulose nanofiber intermediary to fabricate highly-permeable ultrathin nanofiltration membranes for fast water purification, Journal of Membrane Science 524 (2017) 174-185.

[3] M. Majumder, N. Chopra, R. Andrews, B.J. Hinds, Nanoscale hydrodynamics: Enhanced flow in carbon nanotubes, Nature 438 (2005) 44-44.

[4] W. Sparreboom, A. van den Berg, J.C.T. Eijkel, Principles and applications of nanofluidic transport, Nature Nanotechnology 4 (2009) 713.

[5] S.K. Bhatia, A.L. Myers, Optimum Conditions for Adsorptive Storage, Langmuir 22 (2006) 1688-1700.

[6] Y. Peng, V. Krungleviciute, I. Eryazici, J.T. Hupp, O.K. Farha, T. Yildirim, Methane Storage in Metal–Organic Frameworks: Current Records, Surprise Findings, and Challenges, Journal of the American Chemical Society 135 (2013) 11887-11894.

[7] A.D. Sheehan, J. Quinn, S. Daly, P. Dillon, R. O'Kennedy, The Development of Novel Miniaturized Immuno-sensing Devices: A Review of a Small Technology with a Large Future, Analytical Letters 36 (2003) 511-537.

[8] E.E. McLeary, J.C. Jansen, F. Kapteijn, Zeolite based films, membranes and membrane reactors: Progress and prospects, Microporous and Mesoporous Materials 90 (2006) 198-220.

[9] J. van den Bergh, W. Zhu, J. Gascon, J.A. Moulijn, F. Kapteijn, Separation and permeation characteristics of a DD3R zeolite membrane, Journal of Membrane Science 316 (2008) 35-45.

[10] E. Secchi, S. Marbach, A. Niguès, D. Stein, A. Siria, L. Bocquet, Massive radius-dependent flow slippage in carbon nanotubes, Nature 537 (2016) 210-213.

[11] S. Iijima, Helical microtubules of graphitic carbon, Nature 354 (1991) 56-58.

[12] V.I. Isaeva, L.M. Kustov, The application of metal-organic frameworks in catalysis (Review), Petroleum Chemistry 50 (2010) 167-180.

[13] P. Selvam, S.K. Bhatia, C.G. Sonwane, Recent Advances in Processing and Characterization of Periodic Mesoporous MCM-41 Silicate Molecular Sieves, Industrial & Engineering Chemistry Research 40 (2001) 3237-3261.

[14] M. Knudsen, Die Gesetze der Molekularströmung und der inneren Reibungsströmung der Gase durch Röhren, Annalen der Physik 333 (1909) 75-130.

[15] M. v. Smoluchowski, Zur kinetischen Theorie der Transpiration und Diffusion verdünnter Gase, Annalen der Physik 338 (1910) 1559-1570.

[16] R.B. Evans III, G.M. Watson, E.A. Mason, Gaseous Diffusion in Porous Media at Uniform Pressure, The Journal of Chemical Physics 35 (1961) 2076-2083.

[17] R.B. Evans III, G.M. Watson, E.A. Mason, Gaseous Diffusion in Porous Media. II. Effect of Pressure Gradients, The Journal of Chemical Physics 36 (1962) 1894-1902.

[18] E.A. Mason, A.P. Malinauskas, R.B. Evans, Flow and Diffusion of Gases in Porous Media, The Journal of Chemical Physics 46 (1967) 3199-3216.

[19] P.J.A.M. Kerkhof, M.A.M. Geboers, Analysis and extension of the theory of multicomponent fluid diffusion, Chemical Engineering Science 60 (2005) 3129-3167.

[20] J. Xiao, J. Wei, Diffusion mechanism of hydrocarbons in zeolites—I. Theory, Chemical Engineering Science 47 (1992) 1123-1141.

[21] J.B. Young, B. Todd, Modelling of multi-component gas flows in capillaries and porous solids, International Journal of Heat and Mass Transfer 48 (2005) 5338-5353.

[22] O.G. Jepps, S.K. Bhatia, D.J. Searles, Wall mediated transport in confined spaces: exact theory for low density, Phys Rev Lett 91 (2003) 126102.

[23] S.K. Bhatia, D. Nicholson, Friction based modeling of multicomponent transport at the nanoscale, J Chem Phys 129 (2008) 164709.

[24] S.K. Bhatia, D. Nicholson, Modeling Mixture Transport at the Nanoscale: Departure from Existing Paradigms, Physical Review Letters 100 (2008) 236103.

[25] R. Krishna, J.M. van Baten, Unified Maxwell–Stefan description of binary mixture diffusion in micro- and meso-porous materials, Chemical Engineering Science 64 (2009) 3159-3178.

[26] R. Krishna, J.A. Wesselingh, The Maxwell-Stefan approach to mass transfer, Chemical Engineering Science 52 (1997) 861-911.

[27] R. Krishna, Multicomponent surface diffusion of adsorbed species: a description based on the generalized Maxwell—Stefan equations, Chemical Engineering Science 45 (1990) 1779-1791.

[28] M.R. Bonilla, S.K. Bhatia, The low-density diffusion coefficient of soft-sphere fluids in nanopores: Accurate correlations from exact theory and criteria for applicability of the Knudsen model, Journal of Membrane Science 382 (2011) 339-349.

[29] S. Kirkpatrick, Classical Transport in Disordered Media: Scaling and Effective-Medium Theories, Physical Review Letters 27 (1971) 1722-1725.

[30] S. Kirkpatrick, Percolation and Conduction, Reviews of Modern Physics 45 (1973) 574-588.

[31] V.N. Burganos, S.V. Sotirchos, Diffusion in pore networks: Effective medium theory and smooth field approximation, AIChE Journal 33 (1987) 1678-1689.

[32] S.K. Bhatia, D.D. Do, On the concentration dependence of surface diffusion coefficients in capillary porous materials, Proceedings of the Royal Society of London. Series A: Mathematical and Physical Sciences 434 (1991) 317-340.

[33] S.K. Bhatia, Transport of adsorbates in microporous solids: arbitrary isotherm, Proceedings of the Royal Society of London. Series A: Mathematical and Physical Sciences 446 (1994) 15-37.

[34] S.K. Bhatia, Directional autocorrelation and the diffusional tortuosity of capillary porous media, Journal of Catalysis 93 (1985) 192-196.

[35] P.D. Deepak, S.K. Bhatia, Transport in capillary network models of porous media: theory and simulation, Chemical Engineering Science 49 (1994) 245-257.

[36] S.K. Bhatia, Modeling pure gas permeation in nanoporous materials and membranes, Langmuir 26 (2010) 8373-8385.

[37] M.R. Bonilla, S.K. Bhatia, Multicomponent effective medium-correlated random walk theory for the diffusion of fluid mixtures through porous media, Langmuir 28 (2012) 517-533.

[38] M. Moeini, F. Farhadi, Pore Network Modeling of Nanoporous Ceramic Membrane for Hydrogen Separation, Separation Science and Technology 45 (2010) 2028-2038.

[39] R. Mourhatch, T.T. Tsotsis, M. Sahimi, Network model for the evolution of the pore structure of silicon-carbide membranes during their fabrication, Journal of Membrane Science 356 (2010) 138-146.

[40] F. Chen, R. Mourhatch, T.T. Tsotsis, M. Sahimi, Pore network model of transport and separation of binary gas mixtures in nanoporous membranes, Journal of Membrane Science 315 (2008) 48-57.

[41] F. Chen, R. Mourhatch, T.T. Tsotsis, M. Sahimi, Experimental studies and computer simulation of the preparation of nanoporous silicon-carbide membranes by chemical-vapor infiltration/chemical-vapor deposition techniques, Chemical Engineering Science 63 (2008) 1460-1470.

[42] C. Rieckmann, F.J. Keil, Multicomponent diffusion and reaction in three-dimensional networks: geberal kinetics, Chemical Engineering Science 49 (1994) 4811-4822.

[43] R. Krishna, J.M. van Baten, Insights into diffusion of gases in zeolites gained from molecular dynamics simulations, Microporous and Mesoporous Materials 109 (2008) 91-108.

[44] R. Krishna, J.M. van Baten, Onsager coefficients for binary mixture diffusion in nanopores, Chemical Engineering Science 63 (2008) 3120-3140.

[45] X. Hu, Multicomponent Adsorption Equilibrium of Gases in Zeolite: Effect of Pore Size Distribution, Chemical Engineering Communications 174 (1999) 201-214.

[46] G.J. Tjatjopoulos, D.L. Feke, J.A. Mann, Molecule-micropore interaction potentials, The Journal of Physical Chemistry 92 (1988) 4006-4007.

[47] N.A. Seaton, Determination of the connectivity of porous solids from nitrogen sorption measurements, Ind. Eng. Chem. Res. 36 (1997) 3275-3281.